Atomistic simulation of SrF_2 polymorphs

E. Francisco, M. A. Blanco, and G. Sanjurjo
Departamento de Química Física y Analítica, Facultad de Química, Universidad de Oviedo, E-33006-Oviedo, Spain
(Received 26 July 2000; revised manuscript received 26 October 2000; published 29 January 2001)

Electron gas interionic potentials (EGIP) have been developed to determine the equation of state (EOS) of the cubic (C1) and orthorhombic (C23) polymorphs of SrF_2, including the thermal effects by means of a quasiharmonic Debye model. The zero pressure cell parameter (a_0), lattice energy (E_{latt}), and bulk modulus (B_0) of the C1 phase are computed with errors smaller than 1.2%, 1.2%, and 7.1%, respectively. The predicted EOS is in good agreement with the observed data and satisfies the *universal* Vinet EOS. For the C23 phase, the optimized zero-p cell parameters a, b, and c and the six fractional coordinates are reported and the pressure dependence of a/a_0, b/b_0, and c/c_0 explored by fitting independent modified Vinet EOS's to the computed data. The analysis reveals a greater compressibility of the C23 phase along the b and c axes than along the a direction. Our calculation predicts the C1$\rightleftharpoons$C23 equilibrium to occur at $p_{tr}=3.92$ GPa, which is between the observed values for the C1$\rightarrow$C23 ($p_{tr}=5.0$ GPa) and C23$\rightarrow$C1 ($p_{tr}=1.7$ GPa) phase transitions.

DOI: 10.1103/PhysRevB.63.094107 PACS number(s): 62.50.+p, 61.50.Ks, 64.60.−i, 65.20.+w

I. INTRODUCTION

Due in part to its high-temperature superionic character, the SrF_2 crystal has been the subject of several experimental[1–10] and theoretical[11–15] studies in the past three decades. From the experimental side, phonon dispersion curves,[1,2] specific heat at high[3] and low temperatures,[8] phase diagram,[4,9] thermal expansion,[5] and ionic conductivity[6,7] have been investigated. From the theoretical viewpoint, geometry, cohesive energy, and bulk modulus,[11] equation of state (EOS),[12] electronic structure,[13] ionic conductivity,[14] and temperature dependence of the elastic parameters[15] have been analyzed. All these studies have been performed in the low−pressure cubic (fluorite type, C1) structure of SrF_2. As in other MX_2 crystals, the C1 phase of SrF_2 undergoes a pressure induced transformation to an orthorhombic ($\alpha-PbCl_2$ type, C23) phase. In some compounds, the C23 structure can be retained as metastable at zero-p when the pressure is gradually released once the C1 $\rightarrow$C23 transition has been completed. CaF_2 is a representative example of this type in which the three unit cell lengths of the C23 phase have been measured in a wide range of pressures (0–50 GPa)[16] and also computed through quantum−mechanical and atomistic simulations.[17] In SrF_2, however, the C23 phase has not been retained at zero-p, because the cubic structure is recovered when p is released down to 1.4 GPa.[9] The zero-p non-existence of the C23 structure stresses the interest of a theoretical study to determine the parameters that define its equation of state. Moreover, a theoretical analysis of the $p-V$ data in terms of empirical EOS's can be very useful to select the best set of structural parameters among a series of zero−pressure values extrapolated from high-pressure data.[18]

Our main objectives in this paper are three. First, we want to characterize the zero-p structural and energetic parameters of the C1 and C23 phases of SrF_2. Second, we will determine the EOS's of both structures, with particular attention to the calculation of the bulk modulus (B_0) and its first pressure derivative (B_0') by fitting the computed $p-V$ data to the Vinet *et al.* empirical EOS.[19] We will also check the possibility of using different linear Vinet EOS to quantitatively analyze the different pressure variations of the individual cell parameters. The last objective of this work is to characterize some of the thermodynamic aspects of the C1$\rightarrow$C23 structural transformation.

The rest of the paper has been divided in three parts. In Sec. II, we briefly describe the simulation schemes used in this study. The most relevant results obtained for both the C1 and C23 phases of SrF_2 are presented and discussed in Sec. III. Finally, in Sec. IV we summarize the main conclusions of our work.

II. SIMULATION SCHEMES

The unit cell descriptions of the cubic (C1) and orthorhombic (C23) structures of SrF_2 are collected in Table I. C1 belongs to the $Fm3m$ (225) space group with the cubic unit cell length (a) being the only free geometrical parameter. C23 belongs to the $Pbnm$ (62) space group, characterized by nine parameters: the three unit cell lengths (a, b, c) and the x and y internal coordinates of the three nonequivalent ions, one strontium (Sr) and two fluorines (F_1, F_2). The development of the interionic potentials and the static optimization of the geometry are described in the next two subsections. The thermal model used to account for the lattice vibrations

TABLE I. Structural description of the unit cells of the C1 (β) and C23 (α) phases of SrF_2.

Phase	Cubic, C1	Orthorhombic, C23
Space group	$Fm3m$	$Pbnm$
Cell parameters	$a=b=c$	$a\neq b\neq c$
	$\alpha=\beta=\gamma=90°$	$\alpha=\beta=\gamma=90°$
Atomic positions	Sr (4a) (0,0,0)	Sr(4c)[x(Sr),y(Sr),$\frac{1}{4}$]
	F (8c) ($\frac{1}{4},\frac{1}{4},\frac{1}{4}$)	F1 (4c)[x(F1),y(F1),$\frac{1}{4}$]
		F2 (4c)[x(F2),y(F2),$\frac{1}{4}$]

is briefly discussed in the last subsection.

A. Development of interionic potentials

The interionic potentials used in this work have been generated using the electron gas model (EGM) of Gordon and Kim[20] feeded with quantum-mechanical ionic electron densities (IED) obtained through the *ab initio* perturbed ion method (*ai*PI).[21,22] As the general strategy has been described and used in previous articles,[23,24] we only give here a brief summary. First, the Hartree-Fock *ai*PI equations for each crystallographically nonequivalent ion (say ion i) embedded in the crystalline environment,[21]

$$[H_i^0 + V^{\text{crystal}}]\phi = \left[H_i^0 + \sum_{j(\neq i)} V_{\text{eff}}^j\right]\phi = \varepsilon\phi, \qquad (1)$$

are solved expressing each orbital ϕ in terms of a monocentric basis set. In Eq. (1), H_i^0 is the free-ion Hamiltonian for ion i and V_{eff}^j represents the crystal potential created by ion j. It contains nuclear attraction, Coulombic electronic repulsion, exchange attraction contributions, and a projector operator that enforces the orthogonality between the orbitals of the ion i and the orbitals of the ion j.[25] The relevant output resulting from the solution of the *ai*PI equations are the self-consistent IED's (ρ) for all the ions of the crystal and their self-energies [$E_{\text{self}}(\rho)$]; i.e., the total atomic energies when the ions are described with the crystal-consistent electron densities (ρ).

Once the IED's are available, the electron gas interionic potential (EGIP) between ions i and j, $V^{ij}(R;\rho_i,\rho_j)$, is generated using the EGM.[23,20] Each EGIP is expressed as a sum of four contributions

$$V^{ij}(R;\rho_i,\rho_j) = V^E(R;\rho_i,\rho_j) + V^K(R;\rho_i,\rho_j) + V^X(R;\rho_i,\rho_j) + V^C(R;\rho_i,\rho_j), \qquad (2)$$

where R is the interionic separation between ions i and j and V^E, V^K, V^X, and V^C stand for Coulombic, kinetic, exchange and correlation energy interactions, respectively. $V^E(R;\rho_i,\rho_j)$ is computed exactly as discussed in Ref. 26, and V^I ($I=K$, X, or C) are given by

$$V^I(R;\rho_i,\rho_j) = \int d\mathbf{r}[\rho\epsilon^I(\rho) - \rho_i\epsilon^I(\rho_i) - \rho_j\epsilon^I(\rho_j)], \qquad (3)$$

where $\rho=\rho_i+\rho_j$ and ϵ^I are electron density functionals that can be chosen in several ways.

The reliability of the EGIP's generated by means of this two-step procedure is directly related to the fulfillment of the basic hypotheses of the EGM and the *ai*PI method. In the EGM used here it is assumed that the IED's are spherical and additive. This means that the electron density for the pair $i-j$ is given simply by $\rho=\rho_i+\rho_j$. The spherical character of the ions is also the main approximation of the *ai*PI method. We want to stress, however, that, as presently implemented, it has successfully been used to date in crystals with relative low ioniciy. Its main drawback is found when ions are placed in very low symmetry positions.

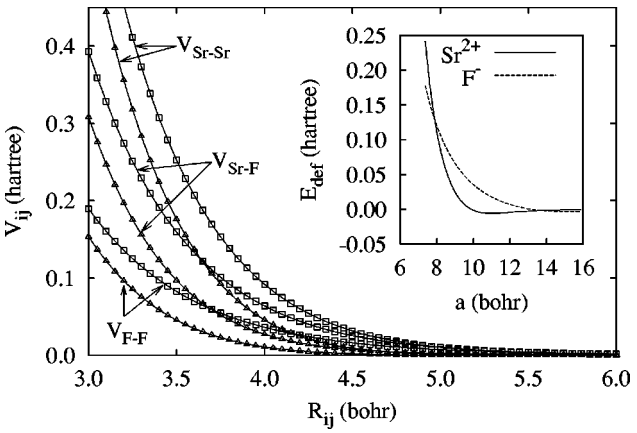

FIG. 1. Sr-Sr, F-F, and Sr-F electron gas interionic potentials for SrF_2 (C1 phase) at lattice parameters $a=7.368$ bohr (△) and $a=15.874$ bohr (□). The inset shows the deformation energy of Sr^{2+} and F^- as a function of a.

Using the above scheme, we have derived the Sr-Sr, Sr-F, and F-F EGIP's in the C1 phase at molecular volumes going from $V=100$ bohr^3 ($a=7.368$ bohr) to $V=1000$ bohr^3 ($a=15.874$ bohr). As basis sets in the generation of the IED's, we have employed the high-quality multi-ζ Slater-type orbitals of by Clementi and Roetti.[27] The Thomas-Fermi, Lee-Lee-Parr,[28] and Lee-Yang-Parr[29] electron density functionals have been used to compute the kinetic, exchange, and correlation energy interactions, respectively. The resulting EGIP's for the Sr-Sr, Sr-F, and F-F pairs (see Fig. 1) become less and less repulsive as the molecular volume decreases. As in the case of the NaCl[23] and MgO[24] crystals, this behavior of the EGIP's is due to the progressive shrinkage of the IED's as the crystal is compressed, and reveals the important reaccommodation of the electron densities to different environments. The use of the EGIP's in atomistic simulations may be facilitated if they are fitted to analytical expressions. This step, however, has been avoided here since there is not a single analytical function that fits the EGIP's at the different crystal geometries with an acceptable root mean square deviation from the input numerical values. Consequently, the numerical interpolation procedure used in Ref. 24 has also been employed in this work.

When EGIP's are used in atomistic simulations, the lattice or cohesive energy of the crystal is given by

$$E_{\text{latt}}(\vec{x}) = \sum_{i<j} V_{ij}(R_{ij};\rho_i,\rho_j) + \sum_i E_{\text{def}}^i(\rho_i), \qquad (4)$$

where R_{ij}, ρ_i, and ρ_j are all functions of $\vec{x}$, the set of parameters that define the crystal geometry. $E_{\text{def}}^{\text{i}}(\rho_i)$ is the total energy of ion i described with the IED ρ_i relative to its gas-phase value. It reflects the deformation suffered by IED's upon crystal formation and collects many-body effects produced by the crystal potential in which the ions are embedded. $E_{\text{def}}^{Sr^{2+}}$ and $E_{\text{def}}^{F^-}$ are shown in the inset of Fig. 1. $E_{\text{def}}^{F^-}$ decreases almost exponentially from 466.8 kJ/mol at $V=100$ bohr^3 down to 48.1 kJ/mol at the zero-p equilibrium geometry of the crystal (a_0). $E_{\text{def}}^{Sr^{2+}}$, though three times

smaller than $E_{\rm def}^{\rm F^-}$ at a_0, increases noticeably for shorter lattice parameters. This behavior contrasts with that of $E_{\rm def}^{\rm Mg^{2+}}$ in MgO[24] (negligible even at lattice parameters as small as 6.0 bohr), and can be due to the more deformable character of the outermost electron shells of Sr^{2+}. It should be emphasized that $E_{\rm def}^{\rm Sr^{2+}}(a_0)$ is negative (-14.4 kJ/mol), which is possible because the correlation energy corrections, computed in the *ai*PI method through the Clementi and Chakravorty formalism,[30] is a nonvariational addition to $E_{\rm def}^{i}$.

We have fitted the analytical expression

$$E_{\rm def}^{\rm i}(a)=A_i e^{-\alpha_i a}+B_i a^{-1} e^{-\beta_i a} \tag{5}$$

to the numerical values of $E_{\rm def}^{\rm Sr^{2+}}$ and $E_{\rm def}^{\rm F^-}$. The fitted parameters $(A_i,\alpha_i,B_i,\beta_i)$ for $E_{\rm def}^{\rm Sr^{2+}}$ and $E_{\rm def}^{\rm F^-}$ are (3397.47, 0.967, -7438.45, 0.815) and (10.455, 0.543, 0.153, 0.0353), respectively. The units for A, B, and (α,β) are Hartree, Hartree$\times$bohr, and bohr^{-1}, respectively.

The last computational aspect concerning the EGIP's is related to the transferability of the C1 EGIP's to the C23 structure. As the physical meaning of the crystal geometry changes with the crystal structure, it is clear that any transferability scheme is necessarily approximate. In two previous works,[23,24] we have transferred the EGIP's generated in the rock-salt (B1) phase to the cesium-chloride (B2) phase taking the molecular volume as the key variable to convey the crystal dependence of the EGIP's and deformation energies from one structure to the other. This scheme worked satisfactorily, probably due to the cubic symmetry of both structures. In the present case, however, the C1 EGIP's transferred to the C23 structure yielded too low values for V_0(C23). Consequently, we derived the C23 EGIP's in a different form. First, $E_{\rm latt}(\vec{x})$(C23) has been fully optimized with respect to all the parameters contained in $\vec{x}$ using the *ai*PI method. Since this optimization is a difficult and very expensive task, not always concluding satisfactorily, the optimum $\vec{x}$ is determined using an iterative procedure: (i) $E_{\rm latt}$(C23) is minimized with respect to a, b, and c, fixing the internal parameters to those found in a previous work on CaF_2;[17] (ii) the internal parameters are optimized fixing a, b, and c to the values found in (i). Steps (i) and (ii) are iteratively carried out until convergence. Second, the equilibrium C23 IED's for Sr^{2+} and F^- are used to derive rigid EGIP's in this phase using the same electron density functionals that were previously employed in the C1 phase.

B. Static optimization of the geometry

At any temperature (T) and pressure (p), the thermodynamic potential necessary to determine the optimal geometrical parameters of a crystalline system is the nonequilibrium Gibbs energy, $G^\star(\vec{x};p,T)$, defined as

$$G^\star(\vec{x};p,T)=E_{\rm latt}(\vec{x})+pV(\vec{x})+F_{\rm vib}(\vec{x};T), \tag{6}$$

where $F_{\rm vib}$ is the vibrational Helmholtz free energy,

$$F_{\rm vib}(\vec{x};T)=\sum_i \left[\frac{1}{2}\hbar\omega_i+kT\ln(1-e^{-\hbar\omega_i/kT})\right], \tag{7}$$

and ω_i are the phonon frequencies. $F_{\rm vib}$ depends on $\vec{x}$ due to the change of the ω_i with the geometry of the crystal. The equilibrium values of $\vec{x}$ at different p and T, $\vec{x}_{\rm opt}(p,T)$, determine the EOS and the Gibbs free energy; i.e., $G(p,T)=G^\star(\vec{x}_{\rm opt};p,T)$. The difficult problem of minimizing $G^\star(\vec{x};p,T)$ with respect to $\vec{x}$ has been simplified in this work by optimizing the geometry in the static approximation,[31] i.e., at $T=0$ and neglecting the zero-point contributions. In these conditions, $G^\star$ transforms to

$$G^\star_{\rm static}(\vec{x};p)=E_{\rm latt}(\vec{x})+pV(\vec{x}). \tag{8}$$

Given that $V=V(\vec{x})$, the equilibrium values of $\vec{x}$ at different pressures, $\vec{x}_{\rm opt}(p)$, determine the static EOS. For the C1 structure, this can be easily obtained through the relation $p_{\rm static}=-(dE_{\rm latt}/dV)$, since in this case $\vec{x}=\{a\}$ and $V=a^3/4$. For the C23 phase, V and $E_{\rm latt}$ are multivariable functions and we must minimize $G^\star_{\rm static}(\vec{x};p)$ with respect to $\vec{x}$ in order to obtain the static EOS. Some preliminary *ai*PI calculations on SrF_2 at $p\neq 0$ have shown that the equilibrium internal parameters are fairly insensitive to pressure, at least in the interval used in this work. Based on these results, we have minimized $E_{\rm latt}(\vec{x})=G^\star_{\rm static}(\vec{x};p=0)$ with respect to all the geometrical parameters contained in $\vec{x}$, but $G^\star_{\rm static}(\vec{x};p\neq 0)$ has been minimized only with respect to a, b, and c.

To apply the thermal model developed in the next subsection, the values of $E_{\rm latt}(V)$ for V's greater than the static zero-p equilibrium volume (V_0) are required. These have been computed in this work by minimizing $G^\star_{\rm static}$ with respect to a, b, and c for negative pressures.

C. Thermal effects

We have used the quasiharmonic Debye model discussed in Ref. 32 to take into account the vibrational effects of the crystal lattice. Given a molecular volume, the Debye temperature, Θ_D, is assumed to be given by[32]

$$\Theta_D=\frac{\hbar}{k_B}[6\pi^2 V^{1/2} r]^{1/3}\sqrt{\frac{B_S}{M}}f(\sigma), \tag{9}$$

where k_B is the Boltzmann constant, M the molecular mass of the crystal, r the number of atoms per molecular unit, B_S the adiabatic bulk modulus of the crystal, σ is the Poisson ratio,[33] and $f(\sigma)$ is given by[33,32]

$$[f(\sigma)]^3=3\left[2\left(\frac{2}{3}\frac{1+\sigma}{1-2\sigma}\right)^{3/2}+\left(\frac{1}{3}\frac{1+\sigma}{1-\sigma}\right)^{3/2}\right]^{-1}. \tag{10}$$

We have used in this work $\sigma=0.306731$, obtained from the experimental zero-p elastic constants at $T=4.2$ K reported by Gerlich[34] (the Poisson ratio hardly changes in the whole range of temperatures measured by this author, as its value at $T=300$ K is 0.305214). Although B_S depends on both V and T, we have approximated it by the expression

$$B_S \simeq B_{\text{static}} \simeq V\left(\frac{d^2E_{\text{latt}}(V)}{dV^2}\right), \tag{11}$$

where B_{static} is the static bulk modulus. This reduces Θ_D to a function of V. The thermal EOS, i.e., the equilibrium volume at any T and p values, $V_{\text{opt}}(p,T)$, is obtained by minimizing with respect to V the thermal nonequilibrium Gibbs function, given by

$$G^\star(V;p,T) = E_{\text{latt}}(V) + pV + F_{\text{vib}}(T,\Theta(V)). \tag{12}$$

It should be again emphasized at this point that the thermodynamic Gibbs free energy is only given by the subset of points in the hypersurface of $G^\star(V;p,T)$ characterized by $V=V_{\text{opt}}(p,T)$. In Eq. (12), F_{vib} is the Helmholtz free energy for lattice vibrations as given by the quasiharmonic Debye model

$$F_{\text{vib}}(T,\Theta(V)) = \frac{9}{8}rR\Theta(V) + rRT \times\left[3\ln(1-e^{-\Theta(V)/T}) - D\left(\frac{\Theta(V)}{T}\right)\right], \tag{13}$$

$$D(y) = \frac{3}{y^3}\int_0^y \frac{x^3}{e^x-1}dx. \tag{14}$$

The isothermal bulk modulus is[32]

$$B_T(p,T) = V(p,T)\left(\frac{d^2G^\star(V;p,T)}{dV^2}\right). \tag{15}$$

The experimental p-V data at any T generally obey some empirical EOS. Here, we have considered the Vinet EOS[19] (VEOS) to represent our static or isothermal $p-V$ results. This EOS connects the (p,V) data through the pseudolinear relation

$$\ln\left[\frac{px^2}{3(1-x)}\right] = \ln H = \ln B_0 + A(1-x), \tag{16}$$

where $x=(V/V_0)^{1/3}$, $A=\frac{3}{2}(B_0'-1)$, and V_0, B_0 and B_0' are the zero-p equilibrium volume, bulk modulus, and its first derivative with respect to p, respectively.

III. RESULTS AND DISCUSSION

In the next subsection, we present, discuss, and compare with available experimental data the results of our atomistic simulation for SrF_2 in the C1 (low-pressure) phase. In the second subsection, we perform a similar analysis of the C23 (high-pressure) phase. Finally, in the third subsection we present and discuss our results for the pressure induced C1 $\rightarrow$C23 phase transition.

TABLE II. Zero-p equilibrium properties of SrF_2 (C1 phase). Units for a_0, E_{latt}, (B_S,B_T), and Θ_D, are bohr, kJ/mol, GPa, and K, respectively.

	Static	4.2 K	295 K
a_0	10.984	11.022	11.080
Expt. (Ref. 34)		10.923	10.960
Expt. (Ref. 5)		10.926	10.951
E_{latt}	−2475	−2465	−2477
Ref. 3	−2505		
Expt. (Ref. 41)			−2492
Expt. (Ref. 42)			−2583
B_S	74.12	71.74	67.83
Expt. (Ref. 5)		74.5	70
B_T	74.12	71.74	64.22
Ref. 12 [a]			98.84
Expt. (Ref. 34)		74.55	69.87
Expt. (Ref. 3)			69.67
Expt. (Ref. 43)			71.28
Expt. (Ref. 4) [b]			69.1
B_T'	4.76	4.78	5.09
Ref. 12 [a]			4.68
Expt. (Ref. 4) [b]			5.2
Expt. (Ref. 35)			5.00
Θ_D		356.32	343.82
Expt. (Ref. 34) [c]		379.06	372.29
Expt. (Ref. 8) [d]		385	

[a]Result obtained by fitting the theoretical data of Ref. 12 to the empirical Vinet EOS.

[b]Values obtained by fitting the room-T $p-V/V_0$ experimental data to the Murnaghan EOS.

[c]Values computed exactly from the experimental data of the elastic constants reported by Gerlich (Ref. 34), using a spherical average of the three components of the sound velocity. These, in turn, may be obtained by solving the Christoffel equations of the crystal (Ref. 36).

[d]Experimental value at 0 K from heat-capacity data.

A. The cubic (C1) phase

1. Zero-p structural and thermodynamic properties

The results for the zero-p equilibrium cell parameter (a_0), lattice energy (E_{latt}), isothermal and adiabatic bulk moduli (B_T and B_S), and pressure derivative of B_T (B_T') of C1 SrF_2 are given along with experimental data in Table II. For comparison reasons, we have also included in the table the B_T and B_T' values that we have obtained by fitting the theoretical atomistic $p-V/V_0$ data of Goyal *et al.*[12] to the empirical Vinet EOS. Our predictions for a_0 and E_{latt} are very good. Both properties differ from the observed values at 295 K by less than 1.1%. The agreement of the computed a_0 with the

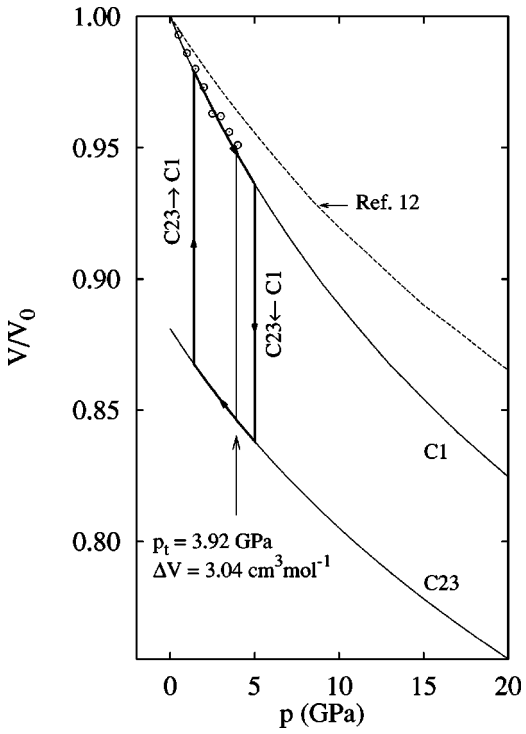

FIG. 2. Equation of state (EOS) of SrF_2 at 300 K. Solid lines stand for our C1 and C23 calculations, while dashed lines stand for the calculations of Goyal *et al.* (Ref. 12). Circles represent the experimental results of Mirwald and Kennedy (Ref. 4). Thick lines represent the experimental hysteresis cycle over our V/V_0 data.

experiment worsens slightly with T, being the errors 0.9% and 1.1% at 4.2 and 295 K, respectively. These differences are enhanced up to 2.8% (4.2 K) and 3.4% (295 K) in the case of V_0 owing to the cubic dependence of the equilibrium volume with a_0. The worsening of the predicted geometry as T increases is due to our computed value of the thermal expansion coefficient, which is to high, as we discuss below.

Our prediction for the heat capacity at constant pressure (C_p) at 20 K and 295 K is 1.031 J/(K mol) and 73.920 J/(K mol), respectively. Experimental values for C_p are available as a polynomial function in the range 2–22 K.[8] At 20 K this functions gives $C_p(20\ \mathrm{K})=1.068$ J/(K mol). Our computed C_p at 20 K agrees well with this value, though this result is not surprising, provided that the Debye model is specially appropriate in the low temperature range.

Our computed value for B_T at 295 K is 7% lower than the value derived by fitting the experimental $p-V/V_0$ data of Ref. 4 to the Vinet EOS. The predicted B_T' is, however, practically coincident with that obtained from this fitting and with the experimental B_T' number reported in Ref. 35. Our prediction for B_T is considerably smaller than the value computed from the atomistic EOS reported by Goyal *et al.*[12] by fitting their $p-V/V_0$ data to the Vinet form. We obtain $B_T=99$ GPa at 295 K from their data, which is $\simeq$32 GPa higher than the experiment and our B_T value. Hence, Ref. 12 predicts a SrF_2 crystal much less compressible than the experiment and our calculations (see Fig. 2). Regarding B_S, our computed values at 4, 300, and 600 K are 71.74, 67.74, and 61.64 GPa. These numbers are about 2–3 GPa lower than the experimentally observed values (74.5, 70, and 64 GPa at 4, 300, and 600 K, respectively).[5]

From our thermal Debye model, we have found $\Theta_D=356$ K and $\Theta_D=344$ K at 0 and 300 K, respectively. These numbers are 6.0% and 7.6% lower than the exact values computed in this work from the experimental data of the elastic constants reported by Gerlich[34] through a spherical average of the three components of the sound velocity. The latter have been obtained by solving the Christoffel equations of the crystal.[36]

We conclude that the computed Θ_D decreases with T faster than the experimental Θ_D does. As a consequence, the Grüneisen constant (γ) derived in this work (2.30) is considerably higher than the experimental result (1.60)[5] and the thermal expansion coefficient (α), obtained in the Debye model as $\alpha=(\gamma C_v/B_T V)$, is also predicted too high: at $T=295$ K, our computed value for α is 8.32×10^{-5} K^{-1}, whereas the experimental value[5] at this temperature is $\alpha_{\mathrm{exp}}=5.43\times10^{-5}$ K^{-1}.

2. The equation of state

We have chosen the usual V/V_0-p curve to represent the crystal response to pressure (Fig. 2). Our theoretical predictions up to 4.5 GPa are in excellent agreement with the experimental EOS of Mirwald and Kennedy[4] and are considerably more accurate than those reported by Goyal *et al.*[12] For example, the experimental V/V_0 ratio at 4.0 GPa is 0.951 GPa,[4] that can be compared with our value (0.947 GPa) and that reported by Goyal *et al.* (0.964 GPa).[12] The pressure induced C23→C1 phase transition, experimentally observed at about 5.0 GPa at 300 K,[9] prevents the analysis of the quality of our results for pressures higher than this value.

The consistency of our simulation can be analyzed by comparing the computed EOS with the *universal* Vinet EOS, that is satisfied by the V/V_0-p data of many real solids. The results of this comparison are illustrated in Fig. 3. The interval of pressures associated to the $1-x$ values displayed in the figure is $0\leqslant p\leqslant200$ GPa. As we can see, the Vinet EOS is very well satisfied by our numerical V/V_0-p data. The correlation coefficient is always better than 0.9997 and improves slightly with T. The values derived for B_0 and B_0' differ from those found numerically by less than 2% and 6%, respectively. These errors are small considering the wide range of pressures used in the fitting.

Thakur and Dwary[37] have shown that the $V/V_0(T)-p$ experimental data of NaCl (rocksalt phase) at different temperatures can be reduced to almost a single curve by plotting $V/V_0(T)$ vs $p/B_0(T)$. This behavior was also showed by previous theoretical results in alkali halides[38] and MgF_2,[32] and also satisfied by our calculations of the C1 phase of SrF_2 (see inset of Fig. 3). The experimental and computed $V/V_0(T)$ values for a given $p/B_0(T)$ ratio are practically independent of T. This is also true in the case of the atomistic results of Goyal *et al.*,[12] despite their very high value for B_0. These facts can be rationalized in terms of the empirical Vinet EOS. From Eq. (16), one can see that, provided that $A=(3/2)(B_0'-1)$ is fixed, $x=(V/V_0)^{1/3}$ is an universal function of $p/B_0(T)$. Two are then the conditions for this *univer-*

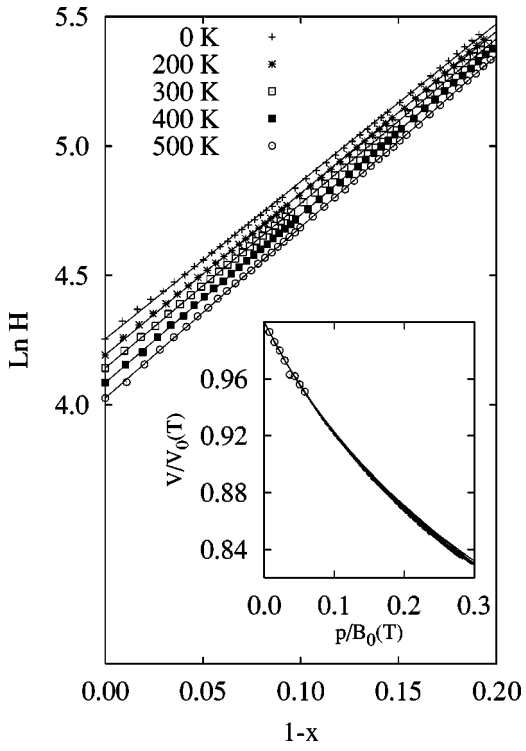

FIG. 3. Vinet EOS of SrF_2 (C1 phase). The $1-x$ data correspond to the pressure range 0–200 GPa. The inset shows the reduced equation of state of SrF_2 (C1 phase) at 0, 100, 200, 300, 400, and 500 K (solid lines), the calculation of Goyal *et al.* (Ref. 12) (dashed line), and the experimental results of Mirwald and Kennedy (Ref. 4) (circles).

sal (T independent) behavior: (i) the empirical Vinet EOS is well satisfied, and (ii) B_0' does not change with T. Experimental data, Goyal *et al* EOS,[12] and our computed $V/V_0(T)-p/B_0(T)$ curves practically coincide due to the fulfillment of the above two conditions and the fact that B_0' is very similar in the three cases.

B. The orthorhombic (C23) phase

1. Equilibrium structure and EOS

This structure is not the most stable at zero-p. In contrast to CaF_2, that has been retained as a metastable phase at 0 GPa after releasing pressure in the experiments performed by Gerward *et al.*,[16] the smallest pressure at which SrF_2 has been detected in the C23 phase is 1.4 GPa.[9] Consequently there are no measurements of the zero-p structural parameters. Our computed values in Table III are, therefore, the first full structural characterization of the orthorhombic phase of SrF_2. The zero-p lattice parameters (a_0, b_0, c_0) computed with the EGIP's are $\sim 4\%$, $\sim 7\%$, and $\sim 7\%$ higher than our *ai*PI results in C23 SrF_2. The latter, in turn, are very close to those found for CaF_2 in Ref. 17. After including thermal effects, the equilibrium volumes of C23 SrF_2 at 0 and 300 K are 3.4 and 4.1 cm^3mol^{-1} smaller than those obtained in the C1 phase.

Regarding the EOS parameters, V_0, B_0, and B_0', it is again important to emphasize that they are unaccessible to the experiment. Thus, our calculation is the only existing guide for a future experimental determination of the high-pressure phase EOS. Our predicted static values for C23 SrF_2 are $V_0=26.15$ cm^3/mol, $B_0=99.4$ GPa, and $B_0'=4.84$ in the EGIP's calculation, being the regression coefficient of the fit to the Vinet EOS of 0.99993. For comparison reasons, *ai*PI results for the same EOS are $V_0=21.71$ cm^3/mol, $B_0=55.4$ GPa, and $B_0'=2.76$. In absence of experimental data, the exceedingly low value of B_0' makes us suspicious about the *ai*PI EOS for this phase. In fact, the value of B_0, almost half that of the EGIP calculation, is *smaller* than that of the less dense C1 phase, contrary to what intuition tell us.

TABLE III. Static zero-p equilibrium properties of SrF_2 (C23 phase).

Parameters	*ai*PI (CaF_2)[a]	*ai*PI (SrF_2)	EGIP's
a_0 (bohr)	13.255	13.304	13.853
b_0 (bohr)	11.142	11.064	11.873
c_0 (bohr)	6.690	6.611	7.126
V_0 (cm^3/mol)	22.04	21.71	26.15
x(Sr)	0.116	0.123	0.112
y(Sr)	0.249	0.247	0.245
x(F1)	0.428	0.432	0.426
y(F1)	0.356	0.354	0.356
x(F2)	0.673	0.674	0.665
y(F2)	0.973	0.968	0.980
E_{latt} (kJ/mol)	−2630	−2543	−2465
B_0 (GPa)	86	55.35	99.44

[a]Reference 17.

We can get more insight into the behavior of B_0 in the C23 phase by exploring the fulfillment of the universal binding energy relation (UBER) discussed in Ref. 39. According to the UBER, the function E_{latt}/E_0 vs V/V_0, where E_0 is the absolute value of E_{latt} at its minimum (V_0), should be universal. In particular, it should be the same for two different phases. Our atomistic simulations reveal that the UBER is only approximately satisfied, since the C23 curve is predicted to be slightly stiffer that the C1 one. This result is probably due to the use of rigid (crystal volume independent) EGIP's in the case of the orthorhombic phase.[24] Assuming, however, that an unique UBER exists for both phases, the relation

$$\frac{B_0(\text{C23})}{B_0(\text{C1})}=\frac{E_{\text{latt}}(\text{C23})}{E_{\text{latt}}(\text{C1})}\,\frac{V_0(\text{C1})}{V_0(\text{C23})} \tag{17}$$

should be satisfied. From the computed static values of E_{latt}(C1), E_{latt}(C23), V_0(C1), and V_0(C23) we have found $B_0(\text{C23})/B_0(\text{C1})=1.126$, and so $B_0(\text{C23})=83.45$ GPa. Even though this number must be taken with caution, due to the nonexact fulfillment of the UBER, the above arguments seem to indicate that B_0(C23) should indeed be greater than B_0(C1), in agreement with our EGIP value, but contrary to the *ai*PI result.

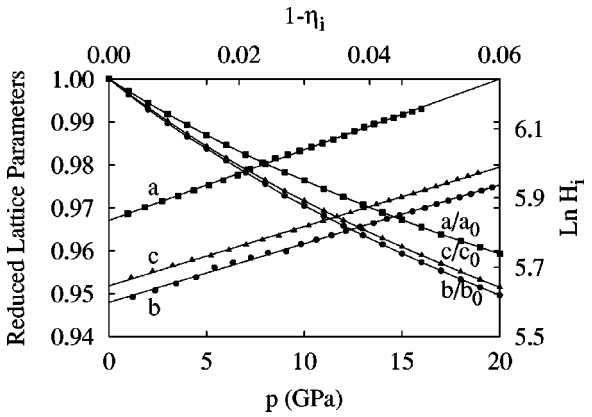

FIG. 4. Pressure dependence of the reduced lattice parameters *a*, *b*, and *c* of SrF_2 (C23 phase). The Vinet EOS fitting for the lattice parameters are shown by the curves labeled a, b, and c, and should be read in the upper and right scales.

2. Pressure anisotropy

The lattice parameters *a*, *b*, and *c* change with *p* as shown in Fig. 4. It is clear from this figure that SrF_2 (C23) can be more easily compressed along the *b* and *c* axes than along the *a* direction. For example, at $p=5$ GPa, *a*, *b*, and *c* are 1.31%, 1.62%, and 1.57% smaller than their respective zero-*p* values. At $p=20$ GPa the reductions with respect to the zero-*p* values are 4.07%, 5.03%, and 4.85%, for *a*, *b*, and *c*, respectively. As a consequence of the greater compressibility of *b* and *c*, the $(b/a,\ c/a)$ ratios decrease from (0.857, 0.514) at 0 GPa down to (0.854, 0.513) at 5 GPa, and (0.848, 0.510) at 20 GPa.

To establish in a more quantitative way the pressure dependence of *a*, *b*, and *c*, the numerical values of these parameters have been fitted by means of a modified Vinet EOS given by

$$\ln H_i = \ln\left[\frac{p\,\eta_i^2}{(1-\eta_i)}\right] = \ln\alpha_i + \beta_i(1-\eta_i), \tag{18}$$

where $\eta_1 = a/a_0$, $\eta_2 = b/b_0$, and $\eta_3 = c/c_0$, and α_i and β_i are fitting parameters (see Table IV). If Eq. (18) is satisfied, the $\ln H_i$ *versus* η_i plot should be linear. This is in fact the observed behavior, as one can see in Fig. 4. The α_i and β_i parameters are related to the linear compressibilities of the crystal, $(d\eta_i/dp)$, as follows. From Eq. (18), we have

$$\left(\frac{d\eta_i}{dp}\right) = \frac{\eta_i^3}{\alpha_i e^{\beta_i(1-\eta_i)} f(\eta_i)}, \tag{19}$$

TABLE IV. Vinet EOS parameters for the lattice constants *a*, *b*, and *c* of SrF_2 (C23 phase).

η_i	α_i(GPa)	β_i
a/a_0	342.05	6.80
b/b_0	270.07	5.65
c/c_0	283.37	5.70

TABLE V. Elastic constants (GPa) of SrF_2 (C23 phase).

C_{11}	188.97	C_{12}	61.19
C_{22}	175.71	C_{13}	64.28
C_{33}	178.79	C_{23}	50.02
B_0	99.33		

where $f(\eta_i) = \eta_i - 2 - \beta_i\eta_i(1-\eta_i)$. At $p=0$, $\eta_i=1$, and $f(1)=-1$, which implies that $(d\eta_i/dp)_0 = -\alpha_i^{-1}$ and

$$B_0^{-1} = -\left(\frac{d(V/V_0)}{dp}\right)_0 = -\sum_i (d\eta_i/dp)_0 = \sum_i \alpha_i^{-1}. \tag{20}$$

This indicates that the α_i parameters are nothing more than the inverse of the zero–*p* linear compressibilities. Furthermore, it is clear from Table IV that the fitting of the η_i *versus p* curves to the Vinet EOS offers a very useful quantitative measure of the (different) responses to pressure of *a*, *b*, and *c* in an arbitrary crystal. Using the α_i values of Table IV and applying Eq. (20), we have obtained B_0(C23) $=98.5$ GPa. This value is consistent with that of Table III, obtained numerically by using Eq. (11).

The ease of compression along different axes can be also quantitatively analyzed in terms of some of the elastic constants of the crystal, C_{ij} $(i,j\leqslant 3)$, where only derivatives with respect to cell lengths are involved

$$C_{ij} = \frac{1}{V_0}\left(\frac{\partial^2 E_{\rm latt}}{\partial\eta_i\partial\eta_j}\right). \tag{21}$$

For the C23 crystalline system, the six independent C_{ij} $(i,j \leqslant 3)$ are C_{11}, C_{22}, C_{33}, C_{12}, C_{13}, and C_{23}. Using the Richardson-iterated, finite-difference formula discussed in Ref. 17 to compute the derivatives involved in Eq. (21), we have obtained the C_{ij} values reported in Table V. These numbers support the conclusions emerging from Fig. 4: SrF_2 (C23) is slightly more compressible along the *a* axis than along the *b* and *c* axes. B_0 is related to the C_{ij} by $B_0 = \frac{1}{9}[C_{11}+C_{22}+C_{33}+2C_{12}+2C_{13}+2C_{23}]$. From this equation, we obtain $B_0=99.33$ GPa, again consistent with the value obtained from Eq. (11) (see Table III).

C. The C1→C23 transition

The pressure induced phase transition among the C1 and C23 structures (commonly known as the $\beta\rightleftharpoons\alpha$ transition) is experimentally observed at 5.0 GPa when increasing pressure at room temperature,[9] i.e., in the $\beta\rightarrow\alpha$ direction. It shows a measurable hysteresis, as the $\alpha\rightarrow\beta$ transition is observed when decreasing pressure, at ~1.4 GPa.[9] The $\beta\rightarrow\alpha$ transformation has also been observed by *in situ* x-ray diffraction experiments by Jamieson and Dandekar.[40] They suggest a reduction of volume of $8.4\pm0.4\%$.[40] Extrapolating at 5 GPa the experimental compression data of Mirwald and Kennedy[4] for the C1 phase (after fitting their $p-V/V_0$ data to the Vinet EOS) and using the zero-*p* value for V_0 (C1) reported by Gerlich,[34] we have computed an *experimental* extrapolated *V* (C1) value at 5.0 GPa equal to 27.58

cm^3/mol. From this value and the reduction of volume suggested by Jamieson and Dandekar, we finally obtain that the *experimental* change of the molar volume at the transition is 2.32 ± 0.2 cm^3mol^{-1} (8.4%), that coincides with the value suggested by Jamieson and Dandekar.[40]

From a theoretical viewpoint, the thermodynamic transition pressure (p_{tr}) is reached when the Gibbs energies of both phases are the same. Due to hysteresis, this situation is achieved before the $\beta \rightarrow \alpha$ (upon compression) and after the $\alpha \rightarrow \beta$ (upon decompression) transitions are observed in the laboratory, that is, for an intermediate pressure. Therefore, the computed p_{tr} must lie in the range 1.4–5.0 GPa. Our results are shown in Fig. 1. Fitting the $\Delta G = G(\mathrm{C23}) - G(\mathrm{C1})$ data to a parabolic expression in p we obtain $p_{tr} = 3.92$ GPa and $\Delta V = 3.04$ cm^3mol^{-1} (10.6 %). At the experimentally observed $\beta \rightarrow \alpha$ transition (5.0 GPa), our computed value for ΔV is 2.96 cm^3mol^{-1} (10.4 %). Though ΔV slightly overestimated in both cases, these results can be considered very satisfactory.

Making again the hypothesis that the UBER is exactly satisfied, a first-order approximation to p_{tr} can be easily derived as[39]

$$p_{tr}^{(1)} = \frac{\Delta E_0}{\Delta V_0}, \tag{22}$$

where Δ represents differences between the C23 and the C1 values. The treatment through a second-order formula gives[39]

$$p_{tr}^{(2)} = -\frac{\Delta V_0 + \sqrt{(\Delta V_0)^2 + 2(\rho/B_0)\Delta(V_0^2/E_0)\Delta E_0}}{(\rho/B_0)\Delta(V_0^2/E_0)}, \tag{23}$$

where $\rho = E_0(\mathrm{C1})/V_0(\mathrm{C1})$ and $B_0 = B_0(\mathrm{C1})$. By applying Eqs. (22) and (23) we have obtained $p_{tr}^{(1)} = 2.82$ and $p_{tr}^{(2)} = 2.72$ GPa, respectively. Higher order values for p_{tr} could be obtained by truncating the series expansion of $E^\star = E_{latt}/E_0$ in terms of $p^* = p/\rho$ at the third, fourth, etc., powers of p^*.[39] Given the experimental transition pressure (5 GPa$\equiv p^* = 0.060$) and the small difference between $p_{tr}^{(1)}$ and $p_{tr}^{(2)}$, we believe, however, that the second-order expansion of G^* is probably accurate enough. The difference of $p_{tr}^{(1)}$ and $p_{tr}^{(2)}$ with respect to the value computed for p_{tr} by solving $\Delta G = 0$ can be attributed to the limitations of the UBER model and also to the fixing of the internal parameters of the C23 phase at $p \neq 0$. As the UBER model only involves zero-p properties, the UBER p_{tr} values will not change if the crystalline geometry at $p \neq 0$ is fully optimized. On the other hand, though the p_{tr} value obtained by solving $\Delta G = 0$ is only approximate, a full optimization of the geometry at $p \neq 0$ will necessarily decrease its value and will probably bring it closer to the UBER p_{tr} value.

IV. CONCLUSIONS

An atomistic model using EGIP's has been applied to study the crystal response to pressure and temperature of SrF_2 in the cubic (C1) and orthorhombic (C23) crystalline phases. The results have been used to determine the zero-p equilibrium geometry, lattice energy, bulk moduli, static and thermal EOS, and the C1$\rightarrow$C23 phase transition data.

The zero-p cell parameter and lattice energy of the C1 phase are computed with errors smaller than 1.2% with respect to the experimental data, while the error in the bulk modulus is lower than 7.2%. Our simulation scheme predicts the orthorhombic structure 10 kJ/mol higher in energy than the cubic one. This result is in qualitative agreement with the experiment and explains the absence of experimental data at zero-p for the C23 phase.

The predicted EOS for SrF_2 in the C1 and C23 phases fit very well the *universal* Vinet EOS, and is in good agreement with the observed data in the case of the C1 structure. It is relevant to mention that the reduced unit cell lengths (a/a_0, b/b_0, and c/c_0) *versus* p data of the orthorhombic phase also satisfy modified Vinet EOS, and we can therefore use them to analyze the different response to pressure of these parameters. This analysis reveals a SrF_2 crystal in the C23 phase more compressible along the b and c axes than along the a direction.

Finally, we predict the thermodynamic transition pressure (p_{tr}) for the pressure induced C1$\rightleftharpoons$C23 transformation to be 3.92 GPa. This result lies between the experimental values for the C1$\rightarrow$C23 ($p_{tr} = 5.0$ GPa) and C23$\rightarrow$C1 ($p_{tr} = 1.7$ GPa) phase transitions, as it should be due to the pressure hysteresis of this type of structural changes. Moreover, our p_{tr} value is very close to a *pseudoexperimental* p_{tr} value that can be derived assuming a similar hysteresis for the direct and reverse phase transformations ($p_{t,exp} = 3.35$ GPa).

ACKNOWLEDGMENTS

We are very grateful to the Spanish Dirección General de Investigación Científica y Técnica (DGICYT), Project No. PB96-0559, for financial support.

[1] J. R. Ferraro, H. Horan, and A. Quattrochi, J. Chem. Phys. **55**, 664 (1971).
[2] M. M. Elcombe, J. Phys. C **5**, 2702 (1972).
[3] C. R. A. Catlow, J. D. Comins, F. A. Germano, R. T. Harley, and W. Hayes, J. Phys. C **11**, 3197 (1978).
[4] P. W. Mirwald and G. C. Kennedy, J. Phys. Chem. Solids **41**, 1157 (1980).
[5] G. K. White, J. Phys. C **13**, 4905 (1980); R. B. Roberts and G. K. White, *ibid.* **19**, 7167 (1986).
[6] A. D. Reed and D. Lazarus, Phys. Rev. B **27**, 6504 (1983).
[7] A. V. Chadwick, Solid State Ionics **8**, 209 (1983).
[8] L. T. Ho, D. P. Dandekar, and J. C. Ho, Phys. Rev. B **27**, 3881 (1983).
[9] G. A. Kourouklis and F. Anastassakis, Phys. Rev. B **34**, 1233 (1986).
[10] G. A. Evangelakis and D. Miliotis, Phys. Rev. B **36**, 4958 (1987).

[11] N. Dutt, A. J. Kaur, and J. Shanker, Phys. Status Solidi B **137**, 459 (1986).
[12] R. P. Goyal, O. P. Gupta, and B. R. K. Gupta, Phys. Status Solidi B **146**, 475 (1988).
[13] R. A. Evarestov, I. V. Murin, and A. V. Petrov, J. Phys.: Condens. Matter **1**, 6603 (1989).
[14] D. Bingham, A. N. Cormack, and C. R. A. Catlow, J. Phys.: Condens. Matter **1**, 1205 (1989).
[15] R. K. Singh, S. S. Mitra, and C. N. Rao, Phys. Rev. B **44**, 838 (1991).
[16] L. Gerward, J. S. Olsen, S. Steenstrup, M. Malinowski, S. Asbrink, and A. Waskowska, J. Appl. Crystallogr. **25**, 578 (1992).
[17] A. Martín Pendás, J. M. Recio, M. Flórez, V. Luaña, and M. Bermejo, Phys. Rev. B **49**, 5858 (1994).
[18] J. M. Recio, M. A. Blanco, V. Luaña, R. Pandey, L. Gerward, and J. S. Olsen, Phys. Rev. B **58**, 8949 (1998).
[19] P. Vinet, J. H. Rose, J. Ferrante, and J. R. Smith, J. Phys.: Condens. Matter **1**, 1941 (1989).
[20] R. G. Gordon and Y. S. Kim, J. Chem. Phys. **56**, 3122 (1972); Y. S. Kim and R. G. Gordon, Phys. Rev. B **9**, 3548 (1974); Y. S. Kim and R. G. Gordon, J. Chem. Phys. **60**, 4332 (1974).
[21] V. Luaña and L. Pueyo, Phys. Rev. B **41**, 3800 (1990).
[22] V. Luaña, A. Martín Pendás, J. M. Recio, E. Francisco, and M. Bermejo, Comput. Phys. Commun. **77**, 107 (1993); M. A. Blanco, V. Luaña, and A. Martín Pendás, *ibid.* **103**, 287 (1997).
[23] E. Francisco, J. M. Recio, M. A. Blanco, A. Martín Pendás, and L. Pueyo, Phys. Rev. B **51**, 2703 (1995).
[24] E. Francisco, J. M. Recio, M. A. Blanco, and A. Martín Pendás, Phys. Rev. B **51**, 11 289 (1995).
[25] E. Francisco, A. Martín Pendás, and W. H. Adams, J. Chem. Phys. **97**, 6504 (1992).
[26] A. Martín Pendás and E. Francisco, Phys. Rev. A **43**, 3384 (1991).
[27] E. Clementi and C. Roetti, At. Data Nucl. Data Tables **14**, 177 (1974).
[28] H. Lee, C. Lee, and R. G. Parr, Phys. Rev. A **44**, 768 (1991).
[29] C. Lee, W. Yang, and R. G. Parr, Phys. Rev. B **37**, 785 (1988).
[30] S. J. Chakravorty and E. Clementi, Phys. Rev. A **39**, 2290 (1989).
[31] Information regarding availability of the PAIRPOT program can be obtained by writing to A. Martín Pendás (e-mail address: *angel@fluor.quimica.uniovi.es*).
[32] E. Francisco, J. M. Recio, M. A. Blanco, A. Martín Pendás, and A. Costales, J. Phys. Chem. A **102**, 1595 (1998).
[33] J. P. Poirier, *Introduction to the Physics of the Earth's Interior* (Cambridge University Press, Cambridge, England, 1991), ISBN 0-521-38097-9.
[34] D. Gerlich, Phys. Rev. **136**, B1366 (1964).
[35] J. Shanker and J. P. Singh, Phys. Status Solidi B **110**, 697 (1982).
[36] R. A. Robie and J. L. Edwards, J. Chem. Phys. **37**, 2659 (1966).
[37] K. P. Thakur and B. D. Dwary, J. Phys. C **19**, 3069 (1986).
[38] J. M. Recio, A. Martín Pendás, E. Francisco, M. Flórez, and V. Luaña, Phys. Rev. B **48**, 5891 (1993).
[39] A. Martín Pendás, J. M. Recio, E. Francisco, and V. Luaña, Phys. Rev. B **56**, 3010 (1997). [*Note that the minus sign in Eq. (10) of this reference has to be omitted.*]
[40] J. C. Jamieson and D. Dandekar, Trans. Am. Crystallogr. Assoc. **5**, 19 (1969).
[41] D. R. Lide, *Handbook of Chemistry and Physics*, 72 ed. (Chemical Rubber Company, Cleveland, 1991), ISBN 0-8493-0565-9.
[42] J. Shanker, J. P. Singh, and V. C. Jain, Physica (Utrecht) **B106**, 247 (1981).
[43] S. Alterovitz and D. Gerlich, Phys. Rev. B **1**, 2718 (1970).